Atmospheric Research 271 (2022) 106127

Contents lists available at ScienceDirect

Atmospheric Research

journal homepage: www.elsevier.com/locate/atmosres

A case study of a severe hailstorm in Mendoza, Argentina, during the RELAMPAGO-CACTI field campaign

Hernán Bechis [a,b,c,*], Victoria Galligani [a,b,c], Milagros Alvarez Imaz [a,d], Maite Cancelada [a,c], Inés Simone [a,b,c], Franco Piscitelli [a,b,c], Paula Maldonado [a,d], Paola Salio [a,b,c], Stephen W. Nesbitt [e]

[a] Universidad de Buenos Aires, Facultad de Ciencias Exactas y Naturales, Departamento de Ciencias de la Atmósfera y los Océanos, Buenos Aires, Argentina
[b] CONICET – Universidad de Buenos Aires, Centro de Investigaciones del Mar y la Atmósfera (CIMA), Buenos Aires, Argentina
[c] CNRS – IRD – CONICET – UBA, Instituto Franco-Argentino para el Estudio del Clima y sus Impactos (IRL 3351 IFAECI), Buenos Aires, Argentina
[d] Servicio Meteorológico Nacional, Buenos Aires, Argentina
[e] Department of Atmospheric Sciences, University of Illinois at Urbana-Champaign, IL, USA

ARTICLE INFO

Keywords:
RELAMPAGO
Hailstorm
Severe weather
Remote Sensing

ABSTRACT

Storms in central Argentina are known for producing large and severe hail. Environmental conditions and strong interaction with topography in this region provide unique conditions for the initiation and intensification of severe storms. The RELAMPAGO (Remote sensing of Electrification, Lightning, And Mesoscale/microscale Processes with Adaptive Ground Observations) and CACTI (Clouds, Aerosols, and Complex Terrain Interactions) field campaigns deployed between October 2018 and April 2019 over west-central Argentina have collected unprecedented periods of intensive observation in the region. During the Intense Observation Period (IOP) number 10 (November 26, 2018), 4 cm diameter hail was reported over wide areas of the province of Mendoza. This was the first time a severe hailstorm was measured with multi-platform observations in Mendoza as the IOP deployment included multiple atmospheric soundings, observations from the Center for Severe Weather Research (CSWR) Doppler on Wheel radars (DOWs) and high temporal resolution satellite data from the Advanced Baseline Imager (ABI) and the Geostationary Lightning Mapper (GLM) onboard GOES-16. High-temporal frequency soundings and surface observations collected prior to the convection initiation are analyzed, allowing a detailed description of the pre-convective environment. The establishment of the upslope flow and the role of boundary layer processes that resulted in the development of the severe hailstorm are also analyzed. In addition, several GOES-16 ABI and GLM derived products are investigated, in order to test their ability to forecast convective initiation and provide hail proxies in the region.

1. Introduction

The continental region east of the Andes, covering the north and centre of Argentina, south of Brazil, Paraguay and Uruguay, usually referred to as South Eastern South America (SESA), is known for the occurrence of extreme deep moist convection. Satellite observations indicate that these thunderstorms are among the most intense and deepest in the world (Zipser et al., 2006), as well as efficient high impact weather producers in terms of hail, extreme lighting, damaging winds and heavy rainfall (Matsudo and Salio, 2011; Mezher et al., 2012; Bang and Cecil, 2019; Peterson, 2021). These storms develop under a variety of storm modes in the lee of unique continental-scale and mesoscale topography (Rasmussen and Houze, 2016; Mulholland et al., 2018; Cancelada et al., 2020). SESA's unique meteorological conditions, weather phenomena and geography has awoken interest among the global scientific community and motivated the Remote sensing of Electrification, Lightning, And Mesoscale/microscale Processes with Adaptive Ground Observations (RELAMPAGO) field campaign (Nesbitt et al., 2021), and the Department of Energy Atmospheric Radiation Measurement (DOE-ARM) Cloud, Aerosol and Complex Terrain Interactions (CACTI) field program (Varble et al., 2021). RELAMPAGO mobile operations took place mainly during an intensive operational

* Corresponding author at: Universidad de Buenos Aires, Facultad de Ciencias Exactas y Naturales, Departamento de Ciencias de la Atmósfera y los Océanos, Buenos Aires, Argentina.
E-mail address: hernan.bechis@cima.fcen.uba.ar (H. Bechis).

https://doi.org/10.1016/j.atmosres.2022.106127
Received 7 September 2021; Received in revised form 2 March 2022; Accepted 3 March 2022
Available online 7 March 2022

period from 1 November to 16 December 2018, over two small regions shown in Fig. 1: over and east of the Sierras de Córdoba range and at the Andes foothills, near San Rafael city in the province of Mendoza. Readers are encouraged to refer to Nesbitt et al. (2021) and Varble et al. (2021) for a detailed review of the supporting literature, the instrument deployment and further details about the campaign objectives.

Various studies have shown that these two areas are prone to hail (e.g de la Torre et al., 2011; Sánchez et al., 2009; Mezher et al., 2012; Bruick et al., 2019). Cecil and Blankenship (2012) and Bang and Cecil (2019) through passive microwave observations document a frequency of 10–30 hailstorms per year in central Argentina. Mezher et al. (2012) conducted a report-based hail climatology for Argentina and found that the main area of frequent hail was in Mendoza and that it extended east towards Córdoba and the central plains of Argentina, that is, over the two domains covered by the RELAMPAGO-CACTI deployment (Fig. 1). Kumjian et al. (2020) documents the occurrence of a gargantuan hail event in Córdoba before RELAMPAGO and analyzes the environments of those types of hailstorms. In the province of Mendoza, hailstorms cause significant damage to property and to the regional agricultural economy, with losses of 10% of the total annual agricultural production (Rosenfeld et al., 2006). Large hail (>2 cm) was found to cause 80% of the agricultural damages in the region through only 2–3 events annually (Pérez and Puliafito, 2006). Due to hail damage to the high-value grape crop, hail mitigation experiments began in the 1960s (Grandoso and Iribarne, 1963) and is a common practice nowadays (Makitov, 1999) by the Dirección de Agricultura y Contingencias Climáticas (DACC - Spanish for the Agriculture and Climate Contingencies Agency) of the province of Mendoza.

Hailstorms in Argentina are found to have an annual cycle similar to the United States, with the maximum hailstorm activity occurring during the spring and summer Mezher et al. (2012). However, the climatologies generated by satellite-based methods show an extended diurnal cycle, compared to that found in the United States, with a substantial portion of the distribution occurring during the overnight period (Bruick et al., 2019).

The synoptic environment and mechanisms leading to convection with extreme characteristics in Mendoza bear some similarities to those found in other regions of the world, such as the highly studied plains east of the Rocky Mountains in the United States. The transport of warm and moist air masses from lower latitudes into the region is favoured in summer by the circulation associated with the presence of the thermally-driven Northwestern Argentinian Low (NAL, Seluchi et al., 2003; Saulo et al., 2010), and on occasions is enhanced by moisture and heat transport by the low-level jet (Salio et al., 2002; Marengo et al., 2004; Vera et al., 2006). The enhancement of the NAL, together with an upper-level disturbance advancing from the Pacific Ocean often increases the potential instability and deep vertical wind shear, providing an environment favourable for organized convection (Salio et al., 2007) and hailstorms (Bruick et al., 2019; García-Ortega et al., 2009). The presence of the topography is a key factor in the development of these storms during the warm season and is responsible for the convection initiation (CI) hotspots found by Rosenfeld et al. (2006) and Cancelada et al. (2020) over southern Mendoza. Upslope flow associated with the easterly winds at the southern end of the NAL aids the CI. Also, the diurnal valley and slope wind circulations associated with the complex terrain and the presence of mountain waves (de la Torre et al., 2004; de la Torre et al., 2011; Hierro et al., 2013; de la Torre et al., 2015) may provide additional triggering mechanisms necessary for storm initiation. Furthermore, CI may also be favoured by zones of enhanced moisture flux convergence at the exit region of the low-level jet or by frontal passages (Teitelbaum and D'Andrea, 2015).

Most of the studies that have focused on convective activity in the Mendoza Province have made use of radar data provided by the DACC. These data consist of measurements from two non-coherent S-band radars located in Tunuyán (33.44° S - 68.96° W) and San Rafael (34.65° S - 68.32° W) cities, and a dual-frequency S/X-band non-coherent radar in San Martín (33.07° S - 68.46° W). While these radars are extremely useful for the detection of potential hail-producing cells, some limitations arise from the lack of Doppler velocity and polarized measurements that allow a more complete description of the storm's microphysics and dynamics. Studies have thus not been undertaken to characterize the convective modes associated with hailstorms in the

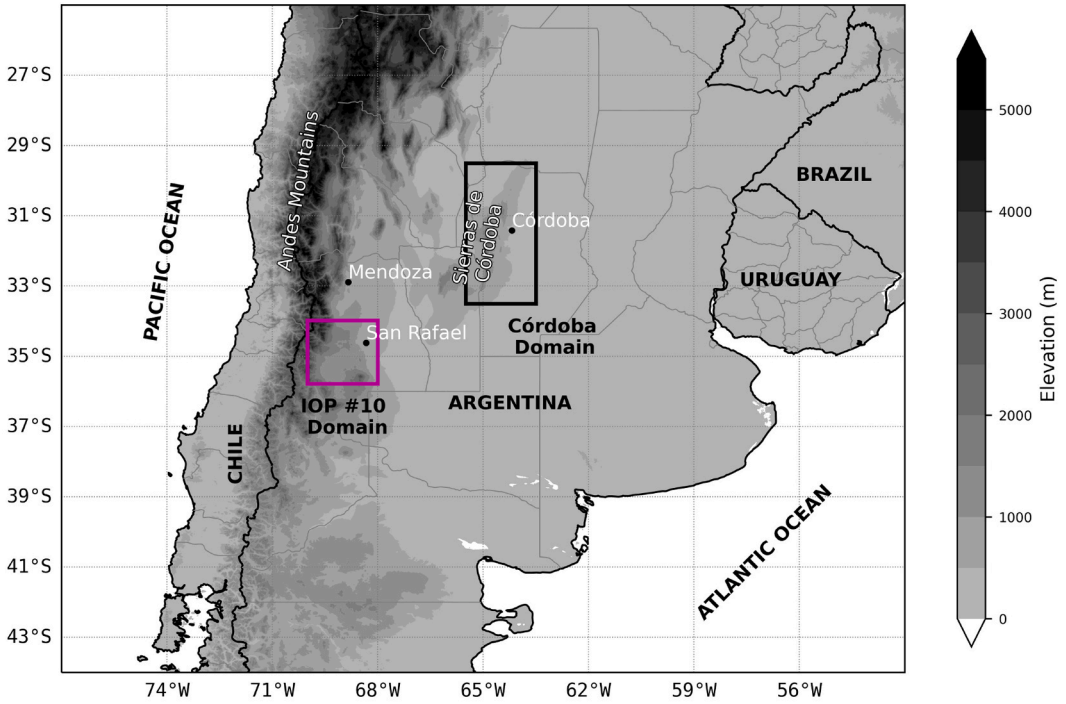

Fig. 1. Location of IOP #10 observational domain (magenta box), the main RELAMPAGO domain in Córdoba (black box), and geographical references. Terrain elevation (AMSL) is shaded. (For interpretation of the references to colour in this figure legend, the reader is referred to the web version of this article.)

region, as the identification of rotating updrafts characteristic of supercells is not possible with the available observations. The satellite-based study of Bruick et al. (2019) suggests that hail producing storms in SESA tend to be multicellular, in contrast with the predominant discrete cells in the United States. Their results however arise from the statistical analysis of storms, from Precipitation Radar (PR) onboard the Tropical Rainfall Measurement Mission. This radar has a 4 km horizontal resolution, reducing the possibility of supercell detection and is necessary to consider that the San Rafael area is located on the border of the PR overpass.

During the field campaign, most of the IOP's were assigned to locations in the Sierras de Córdoba domain due to forecast and logistic considerations, and there were only 2 days (Nov. 25 and 26, 2018) in which the assets travelled to and were deployed in the Mendoza domain. In both cases, severe storms were observed near San Rafael city, although it was during the second day of observations (IOP #10) when the most complete set of observations was collected and severe hail was observed, motivating its selection as a case study. On that day, a group of storms initiated in western Mendoza and propagated eastwards, generating a swath of hail damage that affected the city of San Rafael. Hail of up to 4 cm in diameter was reported from different sources: the RELAMPAGO deployed team, social networks, citizen reports and hailpads. One of the storms moved right over the deployed observational network and allowed the collection of an extensive dataset of observations from a wide range of instruments, including dual-polarization radar data from the RELAMPAGO deployed Center for Severe Weather Research (CSWR) Doppler on Wheel radars (DOWs), hourly soundings and surface station measurements. Also, 1-min resolution satellite data from the Advanced Baseline Imager (ABI) and the Geostationary Lightning Mapper (GLM) sensors onboard the Geostationary Operational Environmental Satellite 16 (GOES-16) are available for this case. This is the first time that such a large amount of observations are available over the region, providing a unique opportunity to observe in detail the characteristics of a severe hailstorm in Mendoza.

The aim of this paper is to characterize the modifications in the pre-convective environment that lead to the initiation of this severe hailstorm utilizing the RELAMPAGO unique dataset. We also seek to characterize the different stages of the storm lifecycle and their association with the severity of hail, by combining remote sensing tools and the numerous surface hail reports. Finally, a set of remote sensing derived products are evaluated, including the GLM Flash Extent Density (FED), the maximum overshooting top (OT) probability described in (Khlopenkov et al., 2021) and the X-band Hydrometeor Identification Algorithm (HID) presented in Dolan et al. (2013), to test their ability to detect and/or forecast changes in storm structure and hail occurrence in this particular case, and their potential use in severe weather nowcasting in the region.

2. IOP #10

2.1. Synoptic overview and forecasting remarks

On November 26, 2018, a slow-moving upper-level short-wave trough at 500 hPa, evident in the water vapour (6.2 μm) GOES-16 imagery (Fig. 2a), crossed the Andes during the day and approached central Argentina. Over Mendoza, the flow at 500 hPa had a westerly component, with a wind magnitude of about 30 kt. At low levels (Fig. 2b), a weak cyclonic circulation developed at the lee of the Andes, with northerly winds over eastern Mendoza and weak southerlies to the south and southwest. These northerlies brought warm, moist air associated with extended cloudiness over northern Argentina southward, between the Andes and the Sierras de Córdoba towards Mendoza and San Rafael.

Data from the convection-allowing models (CAMs) available during the campaign was analyzed to determine the type of mission and the exact locations of the assets to be deployed. One of the models consulted

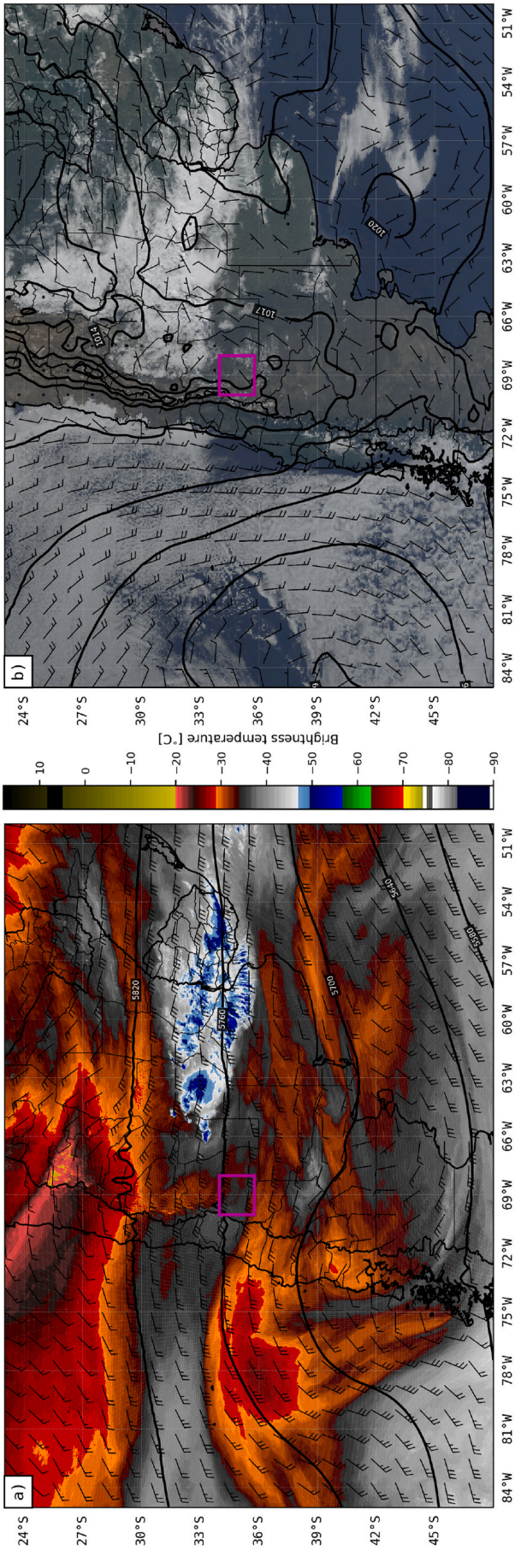

Fig. 2. a) ERA5 geopotential height (contours) and wind at 500 hPa, and brightness temperature from band 8 (6.2 μm) of GOES-16 ABI. b) ERA5 sea level pressure, 10 m wind and GOES-16 ABI true colour image. Valid at 1200 UTC of November 26, 2018. The magenta box indicates the location of the observational domain. (For interpretation of the references to colour in this figure legend, the reader is referred to the web version of this article.)

was the Weather Research and Forecasting version 4 (Skamarock et al., 2019) run by the University of Illinois (UIUC-WRF), initialized at 0000 UTC on Nov. 26 and with boundary conditions taken from the Global Forecast System model. UIUC-WRF had a 3-km horizontal resolution and 51 vertical levels up to 20 hPa and utilizes the Thompson (Thompson et al., 2008) microphysics, YSU (Hong et al., 2006) boundary layer, and RRTMG (Iacono et al., 2008) radiation schemes. Further description of the UIUC-WRF model and other models available during the campaign can be found in Casaretto et al. (2022). The output for the UIUC-WRF shown in Fig. 3(a) illustrates the expected increase of deep-layer shear

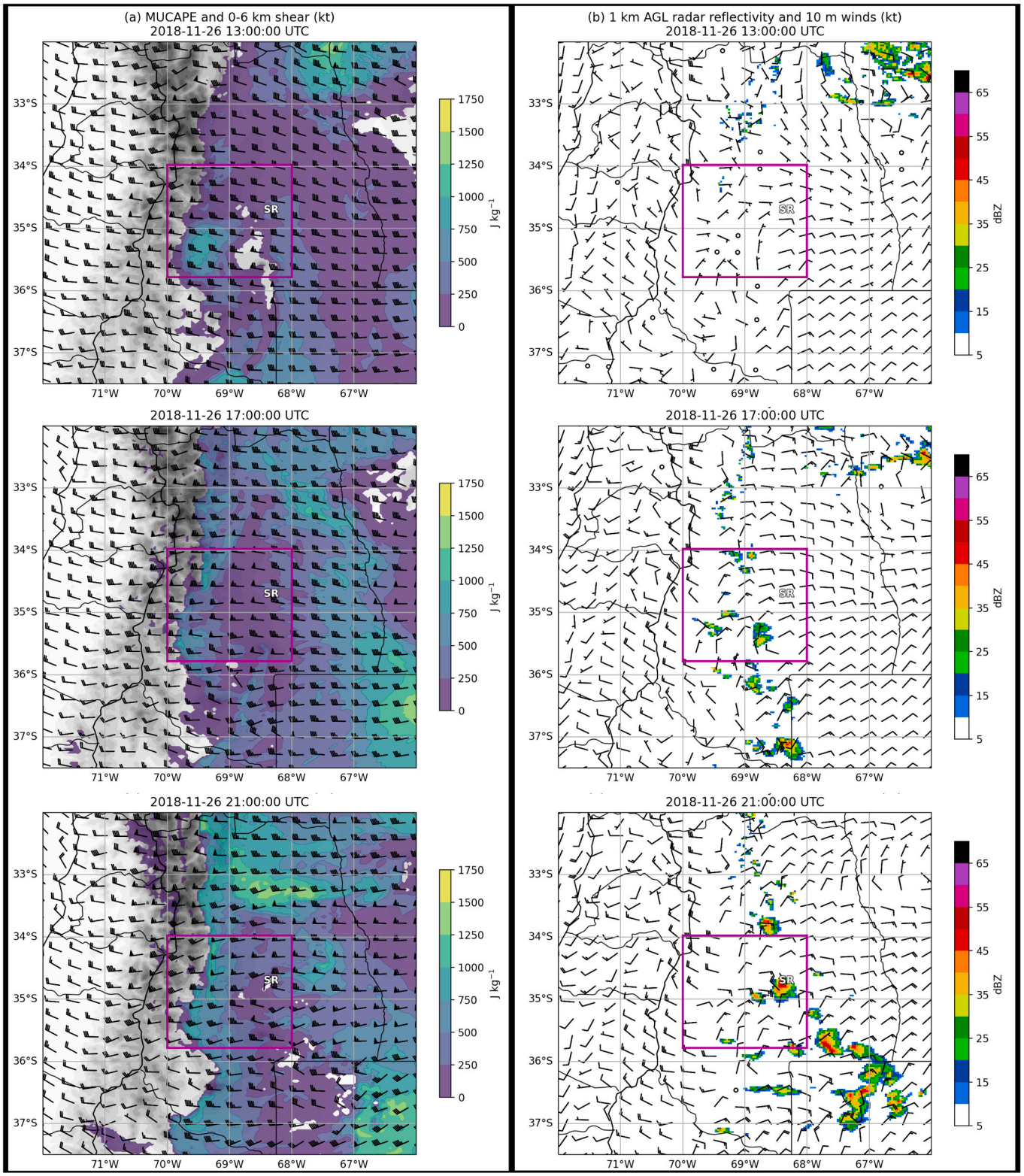

Fig. 3. Evolution of a) Most Unstable CAPE (shaded, J kg^{-1}) and 0–6 km shear (kt, barbs) and b) 1-km AGL reflectivity (shaded, dBz) and 10 m winds (kt, barbs) at 1300 UTC (first row), 1500 UTC (second), and 2100 UTC (third) on November 26, 2018, as forecasted by the UIUC WRF model. The magenta box indicates the IOP #10 domain. (For interpretation of the references to colour in this figure legend, the reader is referred to the web version of this article.)

over the area, associated with the advance of the upper-level shortwave trough, and the larger values of CAPE east of San Rafael, over the lower terrain, also increasing towards the afternoon. The model also anticipated the development of an upslope flow at low levels favouring the CI east of the Andes (Fig. 3b). Several cells were initiated by the model, the most prominent of which was forecasted to pass near the San Rafael city. This cell was also associated in the model with a swath of large values of updraft helicity (not shown), suggesting that the development of a rotating updraft within some of the storms was a possibility (Kain et al., 2008).

With this information, the decision was made that IOP #10 concentrated on CI as the primary mission, and the RELAMPAGO mobile assets were deployed west of San Rafael to a domain roughly centered at 35°S, 69°W (Fig. 4) to capture the CI forecasted to occur around 1500 UTC (1200 LT) close to the slope of the Andes. The asset's disposition also allowed the observation of the potential intensification of the convective cells and possible upscale growth as they moved away from the slope of the terrain, towards the east.

2.2. Observational strategy and deployment

Two DOW X-band (3 cm wavelength) radars were available for this IOP: the dual-polarization DOW-7, and the single-polarization DOW-8 belonging to the CSWR (Wurman et al., 1997). As shown in Fig. 4, the two DOWs were deployed SW of San Rafael, along an SSW-NNE transect with a radar separation of approximately 30 km. Also, three CSWR mobile mesonet vehicles (MMs) were deployed. Two MMs launched soundings along (or near) route 144/40, after dropping portable weather stations (PODs) along this corridor. A third MM placed a line of PODs along route 143 and subsequently made transects along route 150 until rain approached. In total, five teams launched hourly soundings between 1300 UTC (1000 LT) and 1900 UTC (1600 LT) at the locations shown in Fig. 4. The soundings were launched from the two MMs (S1 and S3), and three other portable sounding units belonging to the University of Illinois (U1 and U2) and Colorado State University (CSU). Twelve portable weather stations (PODs) were deployed along the available road network to collect surface parameters as well as those taken by the MMs. Several hailpads were deployed over the domain to supplement the operational hailpad measurement network maintained by the DACC in San Rafael. Additionally, hail diameters were manually measured and a drone aerial photogrammetry study was undertaken (see Soderholm et al., 2020). For instrument characteristics and specifications, readers are encouraged to refer to Nesbitt et al. (2021).

3. Data and methods

The dataset collected during IOP #10 allows us to investigate in this paper different aspects of the storm environment, its internal structure, and its signatures on different remote sensing platforms. Firstly, an overview of the evolution of the storm is provided, using satellite, polarimetric radar data and the in-situ hail reports. The different stages of the storm lifecycle and the size of the hailstones associated with each one are described.

To complement the analysis, we implement the polarimetric-based hydrometeor identification algorithm (HID) developed by Dolan et al. (2013) to the X-band radar observations. This HID is based on one-dimensional fuzzy-logic membership beta functions built from the theoretical scattering simulations and allows the determination of bulk microphysics within a given radar volume. It uses four polarimetric radar observables (attenuation corrected horizontal reflectivity Zh and

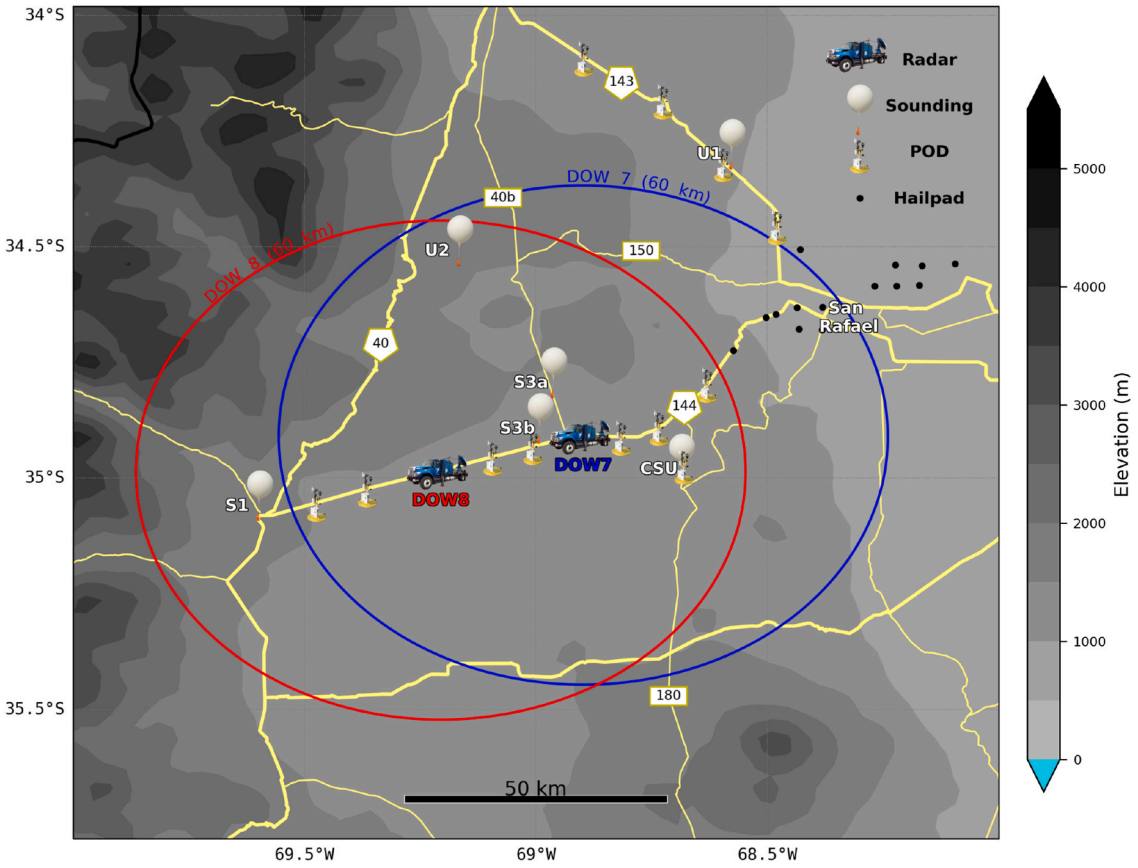

Fig. 4. Location of the mobile assets during IOP #10 on the domain indicated with the black box in Fig. 1. The 60 km range rings from DOW7 and DOW8 radars are shown in blue and red, respectively. In shaded, the height of the topography. (For interpretation of the references to colour in this figure legend, the reader is referred to the web version of this article.)

differential reflectivity ZDR, doppler velocity Vr, specific differential phase Kdp, and correlation coefficient RHOhv) along with the altitude of the freezing level entailing 10 different hydrometeor categories: drizzle, rain, wet snow, dry snow, ice crystals, vertically aligned ice, high-density graupel, low-density graupel, hail, and big drops (>5 mm)/ melting hail. The Python ARM Radar Toolkit (Py-ART, Helmus and Collis, 2016) was used to apply the *Z*-PHI method (Testud et al., 2000) in order to adjust Zh and ZDR for attenuation due to heavy rain. In this study, the temperature was derived from the nearest (in time and distance) available sounding and the hydrometeor with the highest fuzzy logic score was identified as the most probable type at each radar gate. The algorithm has been tested by comparison with S-band polarimetric radars in previous studies showing promise in illustrating bulk hydrometeor types and advantages, especially in the classification of ice hydrometeors and oriented ice crystals over a simple reflectivity- and temperature-only algorithm Dolan et al. (2013). We exploit the high quality of the DOW 7 polarimetric observations to evaluate the results from this HID in comparison with the surface hail reports.

Additionally, the pre-convective environment is investigated with in-situ data. Sequential hourly soundings launched at the location closer to CI and surface meteorological data are presented, to study the processes responsible for the destabilization of the vertical profile. The spatial distribution of the buoyancy and deep layer shear is also analyzed using sounding data, in order to evaluate the variability of these quantities, and their relationship with the different sizes of the hail observed at the surface.

In association with the in-situ and radar measurements deployed by RELAMPAGO, other remote sensing observations collected during the IOP provide a unique opportunity to evaluate the ability of some remote-sensing-derived severe weather proxies to detect and anticipate hail occurrence at the surface. The ABI and GLM sensors onboard GOES-16 (Goodman et al., 2013) allow mapping the total lightning activity (intra-cloud and cloud-to-ground flashes), providing a detailed description of the storm lifecycle. In particular, GOES-16 Mesoscale Domain Sector (MDS) images were available during the entire IOP #10, centered over the region of interest with a 1-min temporal resolution.

The GLM Flash Extent Density (FED) product is analyzed to characterize the evolution of lightning within the storm. This product is a 2×2 km gridded dataset that indicates the number of flashes that occur within a grid cell over a time period that, in this case, is 1 min (Goodman et al., 2019). The implementation of the FED and other GLM products in operational nowcasting provides the opportunity to identify rapid increases in lightning activity, known as lightning jumps, that often precede the development of severe weather (Schultz et al., 2011). While other GLM products like average flash area and total optical energy are available, in this study only FED is evaluated, since it is the one of most popular use among forecasters and the one with the most straightforward interpretation.

In order to characterize the FED evolution of a particular storm of interest, the BAB3T (Backward Adaptive Brightness Temperature Threshold Technique) tracking algorithm developed by Cancelada et al. (2020) is applied to the 1-min GOES-16 10.3 μm infrared observations. This algorithm determines the location of CI for cells of interest and tracks them backwards from a starting point within the observed storm that, in this case, is the pixel with the colder brightness temperature (BT) in the storm of interest at the time of the IOP's end. Later, the FED is evaluated inside the 235 K BT contour associated with the storm of interest, plus a storm environmental "vicinity", resultant from smoothing of the original mask to account for parallax-related differences between the ABI and GLM products that on occasions locate lightning flashes slightly displaced with respect to the cloud shield. Also, some manual corrections are performed when the anvil from nearby storms merge with the main cell, to avoid including in the analysis lightning flashes related to a different cell.

Finally, the existence of overshooting top (OT) signatures and their relationship with hail severity is evaluated. OT's are local minima in the observed IR cloud top temperature, and their presence is indicative of a deep convective updraft strong enough to penetrate through the equilibrium level and into the lower stratosphere, and are often associated with severe weather events (Bedka et al., 2010). To detect the OT's we use the automated detection algorithm developed by Khlopenkov et al. (2021), applied to the 1-min GOES-16 data. This algorithm identifies cold spots embedded within storm anvils and quantifies its tropopause-relative IR BT computed with respect to the MERRA2 reanalysis (Bosilovich et al., 2015), its prominence relative to the anvil, the anvil area, and anvil temperature spatial coherence, to derive the likelihood that it is an OT.

4. Storm evolution

The evolution of the storms during the extent of the IOP #10 from a satellite perspective is shown in Fig. 5. By 1545 UTC a robust cumulus field developed at the slope of the terrain in a North-South oriented line west of San Rafael. CI, defined as the first appearance of a 35 dBZ echo in the radar data, occurred along that line at 1550 UTC southwest of the DOW8 position, near the S1 sounding site shown in Fig. 4). The most prominent storm (hereafter cell "A") initiated at 1616 UTC, and moved right over the observational domain, allowing a detailed collection of hail reports to be recorded. Most reports include the time of observation and photographic evidence (Fig. 6). Two other weaker storms also moved through the IOP's domain. The first one initiated shortly after cell "A" and propagated in an eastward direction. This storm will not be discussed any further in this work, but can be seen in Fig. 5 to the north of cell "A". A second cell (hereafter cell "B") initiated at 1830 UTC west of cell "A" and followed a similar trajectory, although slightly displaced towards the north. Fig. 5 further shows a line of strong cells that developed to the south of the domain, aligned in an NW-SE direction along a weak surface boundary that will also not be analyzed here.

Fig. 7 shows the evolution of the observed low-level plan-position indicator (PPI) of the horizontal reflectivity (Zh) from DOW8, centered in cell "A" between the time of its initiation (1616 UTC) and the time of the last scan of DOW8 at the end of the IOP (1956 UTC). Within the initial stages of its life cycle, the cell merges with another small storm that initiates nearby. As the storm moved to the east, crew members on both DOWs reported "*marble and nickel with a few quarters*" sized hail over DOW8 at 1708 UTC and 2 cm hail over DOW7 at around 1730 UTC. Along the transect between both DOWs, the anemometer on POD-E was damaged, attributable to these hailstones. By 1826 UTC the storm acquired a supercell-like appearance that can be seen in greater detail in Fig. 8 for the 1833 UTC scan, which shows a weak cyclonic rotation in the doppler data indicating the presence of a mesocyclone. The cyclonic rotation is observable during 20 min, and by 1850 UTC it is no longer discernible on doppler data. The supercell then loses its classic structure and evolves into a bigger system that generates several three-body-scattering signatures in the radar Zh data (see Fig. 7), suggesting the presence of hail (Zrnić, 1987; Rauber and Nesbitt, 2018). This is confirmed by the impacts recorded by the hailpads along the track of the storm. In fact, at 1910 UTC, one of the deployed teams reported a 3 cm accumulation of hail on the ground, with the maximum measured in-situ hailstones reaching 4.5 cm. The severe hail swath continued as the storm moved over San Rafael city, where the operational hailpad network reported hailstones of up to 4.75 cm in diameter. Reports of severe hail, with severe property and crop damage, were also found in local newspapers and social media. Finally, near 1930 UTC the storm starts to split, a process that ends with a left-moving dominant supercell that moved outside of the radar range at the end of the IOP. Following the U.S. National Weather Service convention, both small/sub-severe ($\leq$ 2.5 cm) and severe (> 2.5 cm) hail was reported. In general, sub-severe hail was reported sporadically at the initial stages of the cell, while severe hail was reported repeatedly later, after its transition into a supercell. The sections below provide some insight into the possible environmental conditions/storm dynamics that lead to distinct hail distributions.

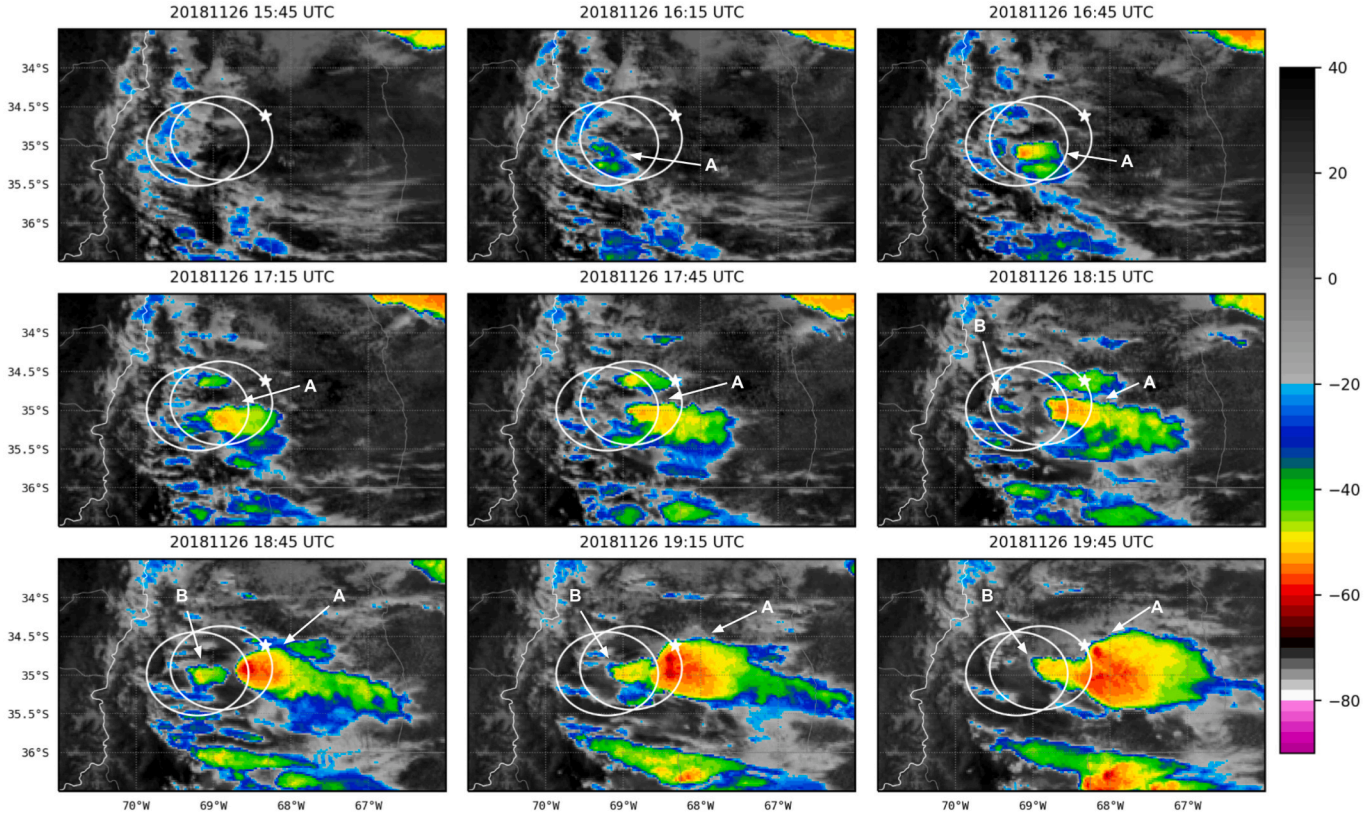

Fig. 5. GOES-16 ABI 10.3 μm brightness temperature depicting evolution of storms "A" and "B" (see text) every 30 min, starting at 1545 UTC. Also shown are the 60 km range rings from DOW7 and DOW8, and the location of San Rafael (white star).

5. Pre-convective environment

The information collected during this IOP allows for a complete description of the pre-storm environment, with sounding data 3 h before the development of an anvil on the storms. The consecutive soundings launched by the S1 team (1590 AMSL, see Fig. 4) between 1300 and 1500 UTC (Fig. 9) provide a clear picture of the modifications in the thermodynamic and wind profiles and are useful to describe the pre-convective environment close to the location where cell "A" initiates. During this period, the wind hodograph shows a small clockwise turn at low levels and a more linear pattern at upper levels with a slight shear increase with time. The upslope-directed easterly and northwesterly component of the wind at low levels is associated with the influence of the deepening of the lee trough. This wind configuration is favourable for storm initiation over the slope of the terrain and further supercell organization (Markowski and Richardson, 2010) and explains the increase of the low-level moisture that is more noticeable at 1500 UTC. From these soundings, the weakening and ascent of the nocturnal inversion are evident, due to the diurnal heating and mixed layer growth that leads to a substantial reduction of the surface-based convective inhibition (CIN). The CIN computed from those soundings decreases from 167 J kg $^{-1}$ to 24 J kg $^{-1}$ between 1300 and 1500 UTC. Also visible in Fig. 9 is the upper-level cooling and concurrent destabilization of the profile as a result of the cold advection aloft and ascent attributable to the advancing shortwave trough. Upper-level moistening at 1500 UTC is also noticeable, associated with some upper-level cloudiness crossing the Andes. Overall, the combined effect of all the processes described above results in a continuous destabilization of the vertical profile at S1 location by reducing CIN and increasing surface-based CAPE (from 3 J kg^{-1} to 274 J kg^{-1}), leading to the observed CI.

In order to understand the nature of the development of the upslope flow that aids the CI, it is necessary to consider the conditions before the first sounding. For that reason, Fig. 10 shows the wind, temperature and dewpoint observations at the location of DOW8, whose mobile mesonet starts measuring near 1130 UTC, 90 min before the first sounding launch. Fig. 10a) shows a clear rotation and intensification of the wind. Initially, weak SSW winds were observed at the surface. The wind progressively rotates towards an easterly and northeasterly (upslope) direction increasing in magnitude as the day progresses, as a result of a slight deepening of the lee trough in the afternoon hours, and the downward transport of easterly momentum aided by strong mixing and associated boundary layer growth. This pattern may be also favoured by the onset of a mountain-plain circulation (Whiteman, 2000), given the cloud-free conditions in the morning and noon (see Fig. 2b) that allows a rapid increase of the temperature (Fig. 10b).

While some not very definite mountain waves were observed in the water vapour imagery during this day (not shown), especially south of the region where the main cell develops, the evolution of the vertical profiles in Fig. 9 and of the surface winds in Fig. 10 suggests that, in this case, other mechanisms (boundary layer mixing, cold advection aloft and the development of the upslope flow) are the most important for the increasing CAPE, decreasing CIN, and eventually leading to convection initiation.

The upper-air observations collected are also useful to characterize the spatial variability of the shear and buoyancy in the environment in which the storm developed. Fig. 11 shows the distribution of the most unstable cape (MUCAPE) and 0–6 km wind shear at 1600 UTC, illustrating the conditions before CI. As expected in a region of complex terrain, there are large differences in those parameters in short distances. The sounding data located closest to the initiation of cell "A" is the westernmost point on the Fig. 11 and exhibits the lowest MUCAPE (358 J kg-1) and 0–6 km shear (42 kt). Towards the East, in the lower terrain, there are much higher MUCAPE values, especially towards the southeast, with 2210 J kg-1 measured by CSU's sounding unit, together

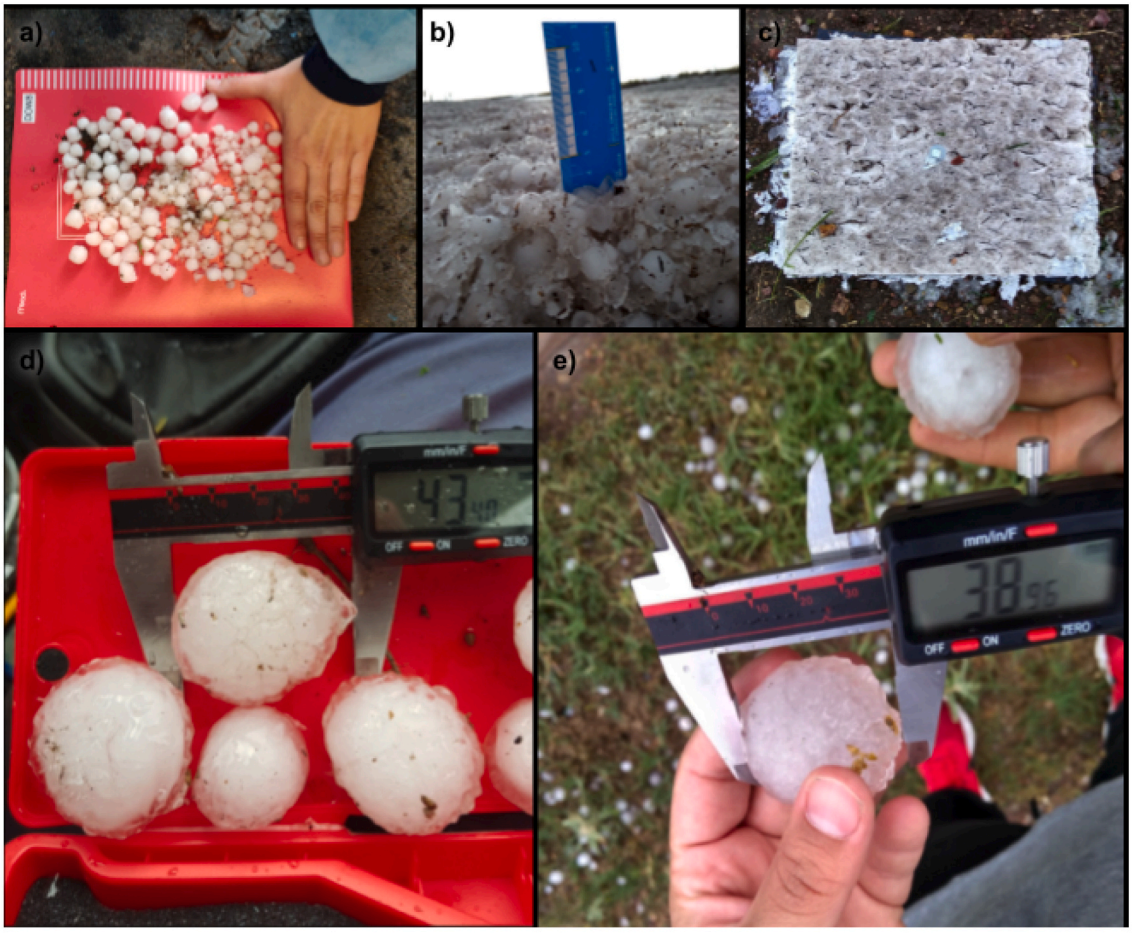

Fig. 6. Pictures of some of the hail reports collected during IOP #10. a) At DOW78 location and b)-e) reports from the "hail team".

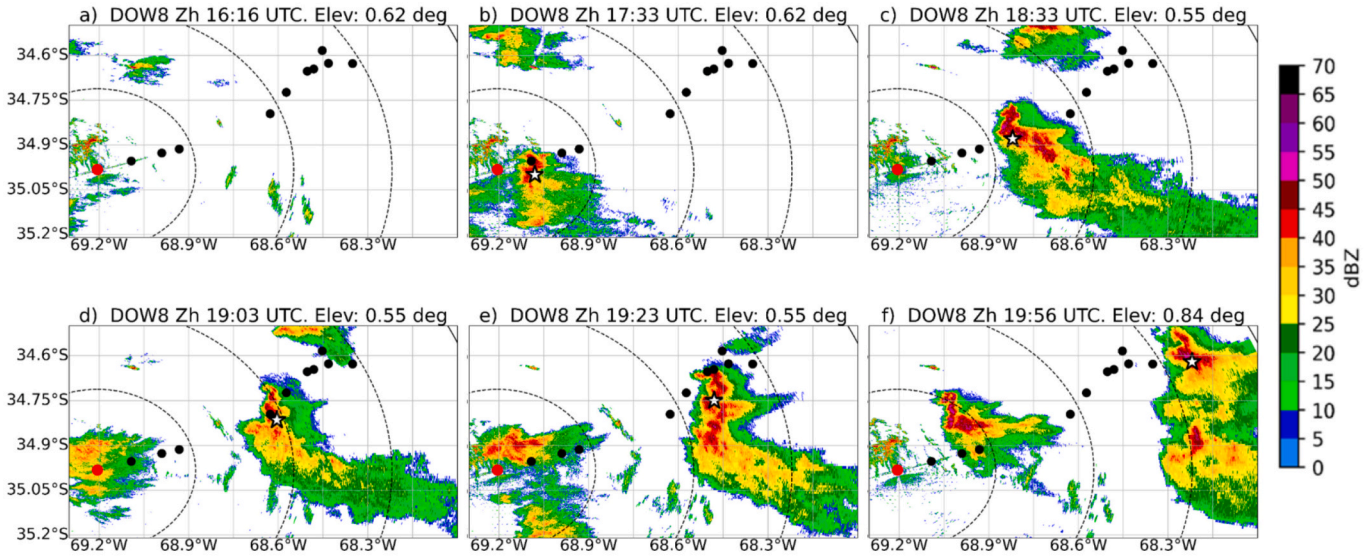

Fig. 7. Evolution of low-level PPI corrected horizontal reflectivity (Zh) from DOW8 covering the period in which cell "A" (marked with a white star) moves over the radar range. The black dots indicate the location of the hail reports at the surface. The red dot indicates the location of DOW 8. (For interpretation of the references to colour in this figure legend, the reader is referred to the web version of this article.)

with an overall larger deep-layer shear ranging between 61 and 71 kt, large enough to support supercell development (Markowski and Richardson, 2010). The low-level anti-clockwise rotation of the wind in Fig. 9 is present to some degree in the other soundings (not shown) and explains the predominance of the left-moving cell after the splitting near the end of the IOP and the overall propagation of cell "A" to the left of the 0–6 km mean wind.

From Fig. 11 it is evident that the environment away from the higher

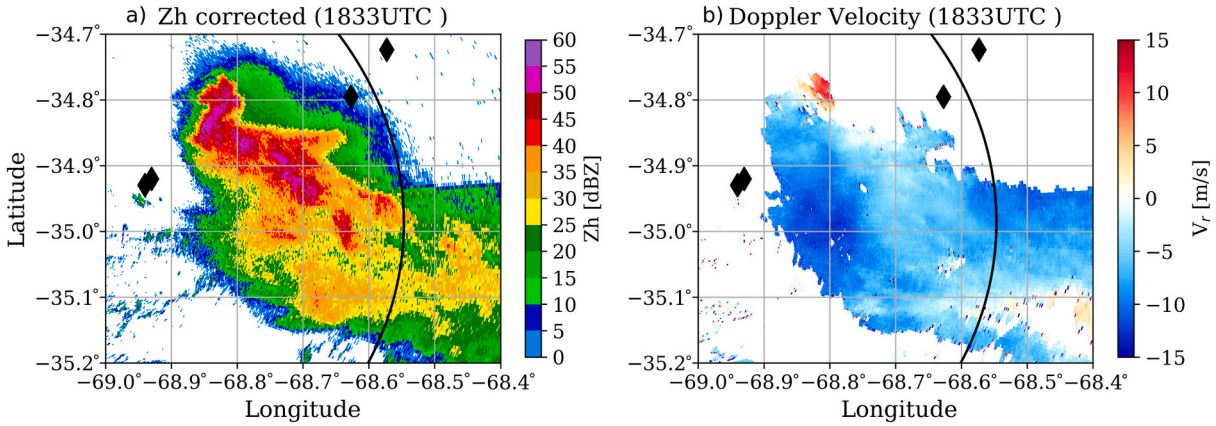

Fig. 8. DOW8 PPI scan at 0.5° elevation of observed horizontal reflectivity (left) and radial velocity (right) at 1833 UTC, centered at cell "A".

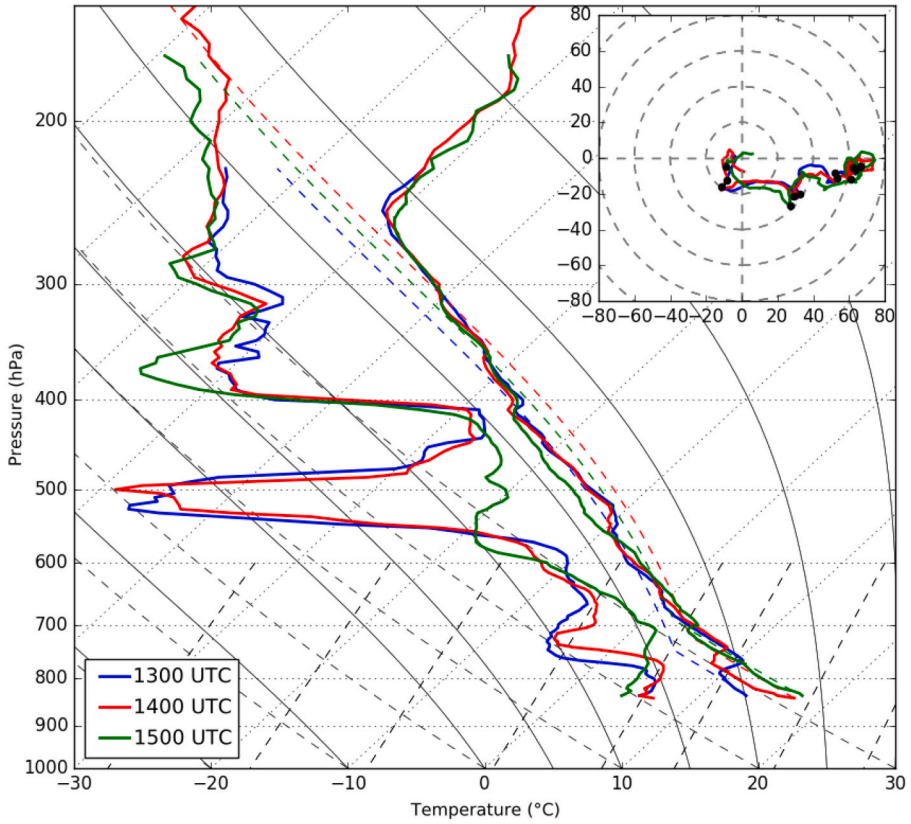

Fig. 9. Upper air measurements from soundings observed at the location of SCOUT 1 before convective initiation, at 1300 UTC (blue), 1400 UTC (red) and 1500 UTC (green). (For interpretation of the references to colour in this figure legend, the reader is referred to the web version of this article.)

terrain is more prone to support supercell development. The IOP observations show that the combined effect of the pressure perturbations associated with rotating updrafts and more buoyant parcels is more likely to contribute to sustaining strong and wider updrafts and, ultimately, larger hailstones than closer to the mountain barrier as shown by (Kumjian and Lombardo, 2020).

6. Hail detection using polarimetric-based HID

The dual-polarization capabilities of DOW 7 allow us to inspect the storm's internal structure further. Fig. 12 shows three stages of the lifecycle of cell "A", as observed by that radar at 1708, 1836 and 1900 UTC. The top row shows the PPI low-level scans of the attenuation corrected Zh, and below each PPI its corresponding pseudo-Range Height Indicator plans (RHI) built from all the available PPI scans for the attenuation corrected Zh and ZDR, RHOhv, and the resultant output from the CSU HID algorithm for different azimuths of interest (black transects in the PPI plans). Although during the period corresponding to the first two times analyzed in Fig. 12 the storm is too close to the radar and hence its structure at higher levels cannot be seen in its totality, we include these RHI plots to contrast its signatures to its latter stage.

At 1708 UTC, Fig. 12a) shows the RHIs for the storm located southwest of DOW 7, close to the position of DOW8 that reported small hail at that time. A small high reflectivity core (>50 dBZ) with shallow vertical development is observed mostly below the freezing level, which at that time is near 2.5 km above the ground, as estimated from the

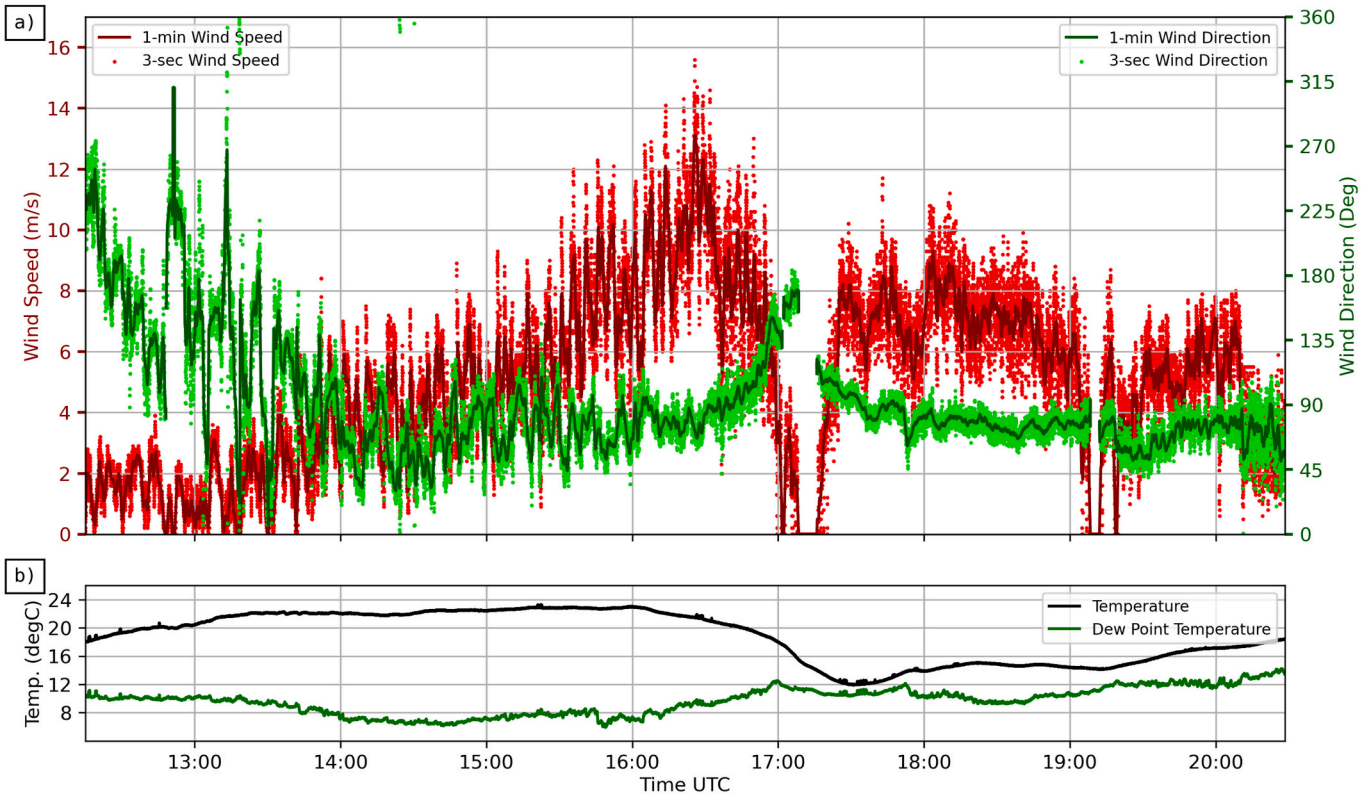

Fig. 10. Time series of a) wind speed (red) and direction (green) and b) Temperature (black) and dew point temperature (green) at the DOW 8 location. The scattered dots and full lines indicate the 3-s and 1-min averages respectively. (For interpretation of the references to colour in this figure legend, the reader is referred to the web version of this article.)

nearby sounding data. Some pixels also show high reflectivity values in the upper part of the storm that reaches a height of about 7 km in this stage. The large Zh values are associated with large ZDR and low RHOhv, especially near the ground, consistent with the presence of large raindrops or melting graupel. This is confirmed by the output of the HID algorithm, which shows mainly the presence of rain below the freezing level, although some hail is detected in some pixels associated with reduced ZDR. This is in accordance with the observations of sporadic small hail at this stage of the storm life cycle. Above the freezing level, mostly high-density graupel is observed, also with some scattered hail signatures.

The next RHI (Fig. 12b) is at 1836 UTC. This time is representative of the period when the storm transitioned into a supercell, as shown in Fig. 8. Fig. 12b) shows signatures for a wider and stronger updraft after the passage of the storm over the radar, which helps explain the increased size in the hailstones reported later. This is also possible because the storm is propagating into a favourable environment to supercell activity (CSU sounding). At this time, the high reflectivity core has increased its depth, and values in excess of 50 dBZ are observed in a large area above the freezing level. In addition, the cell appears to be strongly tilted due to the environmental shear, which increased as it moved east of the Andes and favoured its transition into a supercell. The

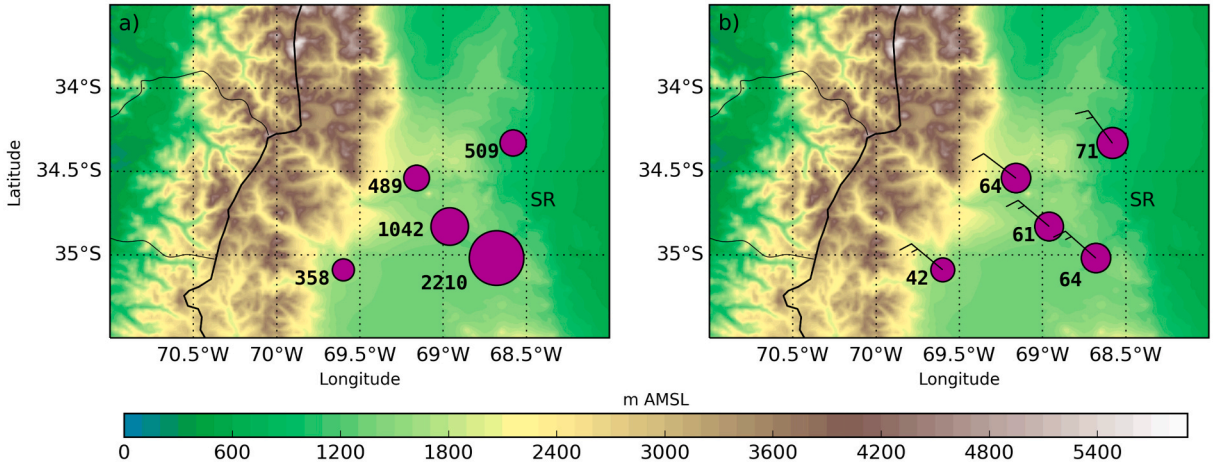

Fig. 11. Distribution of a) MUCAPE and b) 0–6 km shear and mean wind (barbs) obtained by soundings launched at 1600 UTC. In shaded the height of the topography (AMSL).

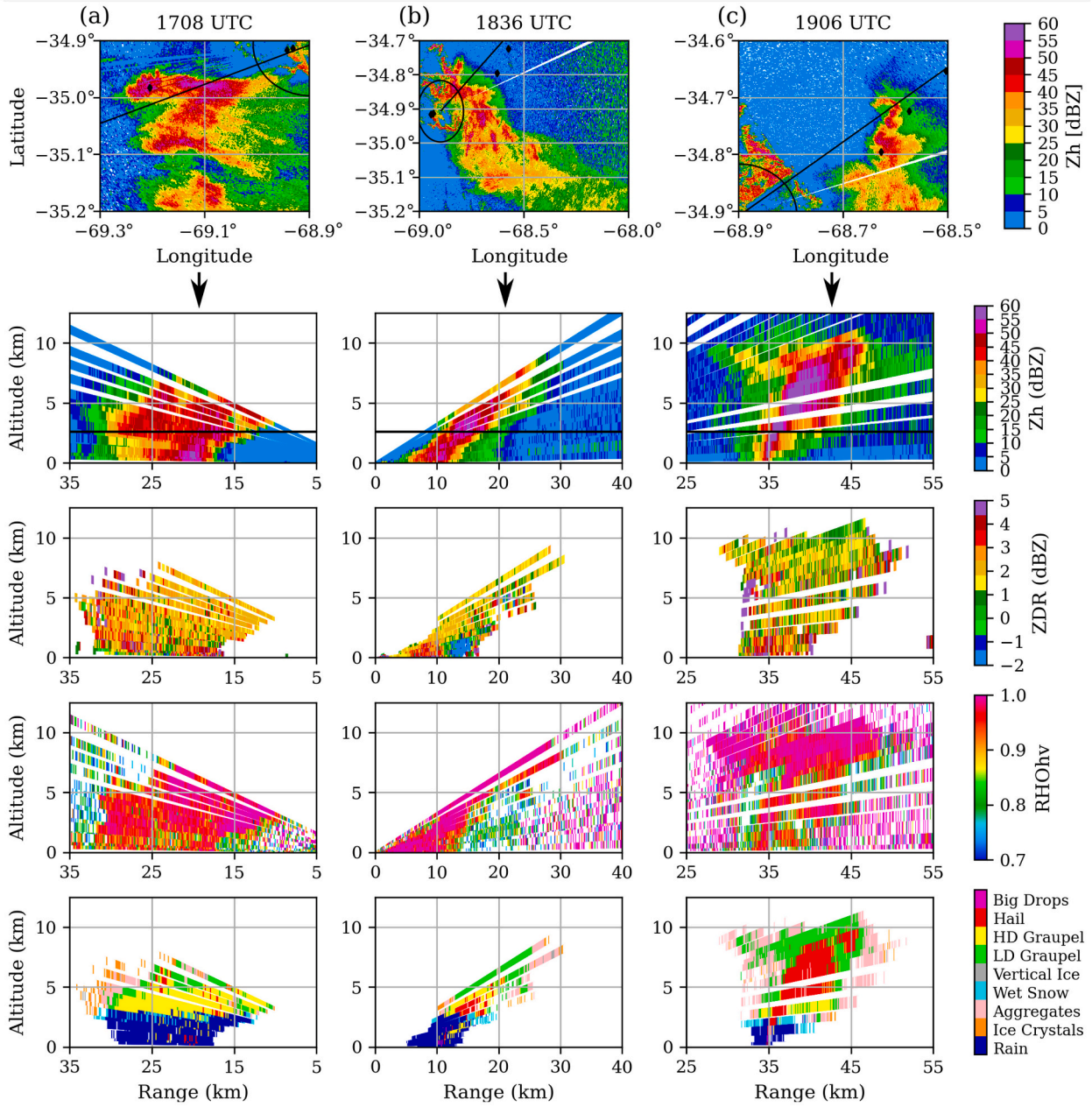

Fig. 12. DOW7 PPI scans at 0.7° elevation of the corrected horizontal reflectivity for a) 1708, b) 1836 and c) 1906 UTC. The column below each PPI shows the constructed RHI scan of variables of interest for the black transect shown in the PPIs. The pseudo RHI is constructed from the available PPI sweeps at each time of interest for attenuation corrected horizontal reflectivity (Zh), corrected differential reflectivity (ZDR), correlation coefficient (RHOhv) and the results from the application of the CSU HID algorithm. The black line in the Zh pseudo RHI plots shows the freezing level height above the terrain as estimated from nearby soundings. In the PPI plans the black dots show the available hail reports and the black circles delimit DOW7 10 km range.

storm's depth has also slightly increased and, although the storm top cannot be completely observed, reflectivities of over 40 dBZ are present at altitudes of nearly 8 km. The high reflectivity values associated with the observed ZDR column (ZDR > 3 dBZ) indicate the presence of an updraft that is lifting to higher levels both liquid and small particles of melting hail. Behind the high reflectivity core, some negative ZDR values are found which indicate the presence of strong differential attenuation, characteristic of short radar wavelength observations, that could not be completely removed by the attenuation correction algorithm considered in the present paper. The HID RHI at 1836 UTC continued to show the presence of rain with hail signatures at the lower levels. However, above the freezing level, there is a larger hail signature surrounded by high-density graupel, evidencing the presence of an embryo curtain around the updraft of the storm (Browning and Foote, 1976; Kumjian and Lombardo, 2020).

By 1906, just before one of the deployed teams reported 3 cm hail accumulation on the ground, signs of a strong updraft were observed (Fig. 12c). The cell denotes a mature stage with a vertical development that reaches 10 km above the ground and a Bounded Weak Echo Region (BWER). The geometry of this scan and the way in which the storm developed no longer leads to strong attenuation, so at 1906 UTC no large negative ZDR values are observed. On the contrary, large ZDR values (close to 4 dBZ) are observed at low levels around the updraft, and also low RHOhv values over the embryo curtain denote the presence of hail. The HID outputs show the abundant presence of hail and graupel that is being ejected away from the main updraft. As mentioned, most hail

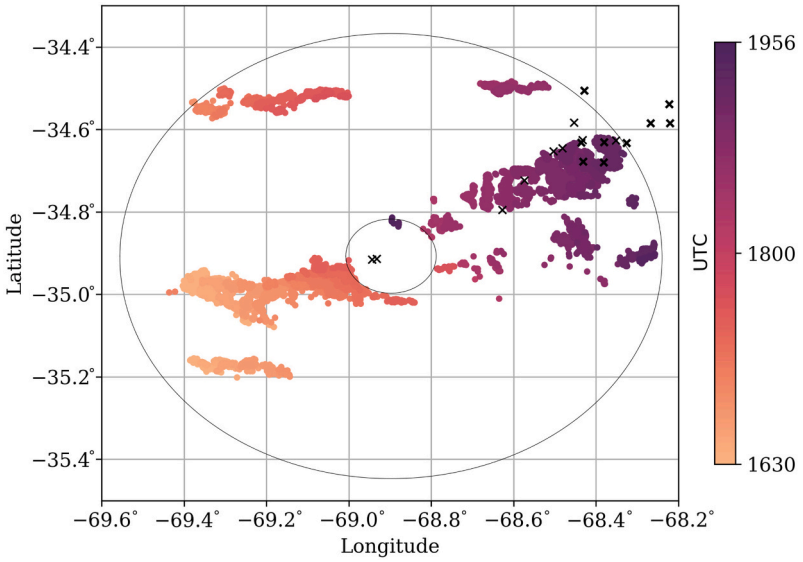

Fig. 13. Temporal evolution of the HID algorithm output using DOW7 (at 2.3°) data indicating the presence of hail in cell "A". The two circles delimit the 10 km and 60 km radar observation range. The black crosses show the available hail reports. The colours represent the UTC time of the radar scan.

reports occurred mainly between 1900 and 1930 UTC. From the cross-sections analyzed here, an evident transition from a weak, shallow storm in the early stages of development to a robust supercell strongly affected by the environmental shear at the latter stages is observed. Initially, only small hailstones are supported, while the wider and stronger updrafts associated with the supercell promote the formation of large and abundant hail.

Finally, in an effort to evaluate the HID algorithm performance in detecting the observed hail and its capabilities to estimate hail occurrence where no in situ reports are available, we present Fig. 13. That Figure shows the location of DOW7 radar gates observing cell "A" at a fixed elevation of 2.3° which results in HID(hail) as a function of time. From Fig. 13 it is possible to observe that hail reports following the passage of cell "A" and the HID algorithm coincide fairly well. It is important to note that the radar does not detect hail when the cell is close or over it, given the effects of attenuation as precipitation falls over the radar and the "cone of silence" effect in which the geometry of the scanning avoids the observation of the storm in its totality. Also noticeable is that, according to the HID, the cell was producing hail prior to its passage over the DOW8 (first in-situ hail report). No reports are available in this low-populated area although the results of the HID algorithm suggest that the cell was producing hail immediately after CI occurs. Given the good performance of the algorithm where observations are available, there is a high probability that small hail was present at those times also.

7. Severe weather satellite based proxies

Fig. 14 summarizes the storm evolution in the period of interest (1630–2000 UTC) from a remote sensing perspective. Fig. 14(a) combines the GOES-16 10.3 μm minimum BT and the maximum flash extent density in the storm for the area corresponding to the BAB3T tracking algorithm described above. Additionally, the grey hail-looking shapes included just above the time axis indicate the existence of hail reports over the storm trajectory (with smaller hail sizes reported before 1800 UTC). The time series of minimum cloud top temperature shows two distinct phases of storm intensification that can be implied from the change in BT with time (i.e., cloud-top cooling rates). At the storm initiation phase, between 1615 UTC and 1640 UTC, large cloud-top cooling rates are observed, consistent with the development of a deep and strong updraft once the cap is removed. After the initial intensification, the minimum cloud top temperature remains stable, between 216 K and 220 K, for a period of almost 2 h. During this period the GLM maximum FED does not show large variations, with values between 2 and 3 flashes/min. Up until this stage, only small hail was reported, with the first report at 1708 UTC, approximately 45 min after initiation, although, as mentioned, the HID algorithm detected hail within the cell as early as 1630 UTC. The second phase of storm intensification takes place between 1830 UTC and 1910 UTC and shows smaller cloud-top cooling rates than those observed during the initial phase. This intensification is coincident with the transition into a supercell described in Section 4 and is preceded by a distinctive peak in electrical activity. A second peak in GLM FED is observed after this period, around 1905 UTC, closer to the time of the most severe hail reports in terms of both size and accumulation (1910 UTC). Note that only hail reports with a trusted time of occurrence are included in this Fig. A large number of hail pads and citizen reports coincide with the passage of this storm after 1900 UTC (see Fig. 7). Fig. 14(b) additionally shows the maximum OT probability in the storm area. As described in Section 3, the OT probability is determined from an automated detection method that uses a combination of spatial IR brightness temperature patterns and modeled tropopause temperature. Following (Khlopenkov et al., 2021), the OT probability can be interpreted as a metric of storm intensity and an estimate of confidence in an OT detection. A rapid increase of the OT probability at 1848 UTC with values reaching above 0.5 indicates the emergence of a GOES-16 10.3 μm pattern associated with OT development. This coincides with the second phase of the storm intensification and occurs about 20 min previous to the most severe hail reports.

While our analysis of the storm is limited to the IOP time frame where radar coverage is available until 2000 UTC, satellite images (not shown) show further cloud-top cooling and the development of a more distinctive OT signature, suggesting that the left-mover supercell continued to intensify after this period. Unfortunately for this study, the storm moved away from the observational domain into a low-populated area northeast of San Rafael, where no severe weather reports were collected.

The results shown in Fig. 14 indicate that the GLM FED has some skill as a forecasting tool, given that the peak in electrical activity detected precedes storm intensification, both in terms of its minimum BT and emerging supercell characteristics as observed by radar. However, caution is advised when attempting to interpret the existence (or lack) of

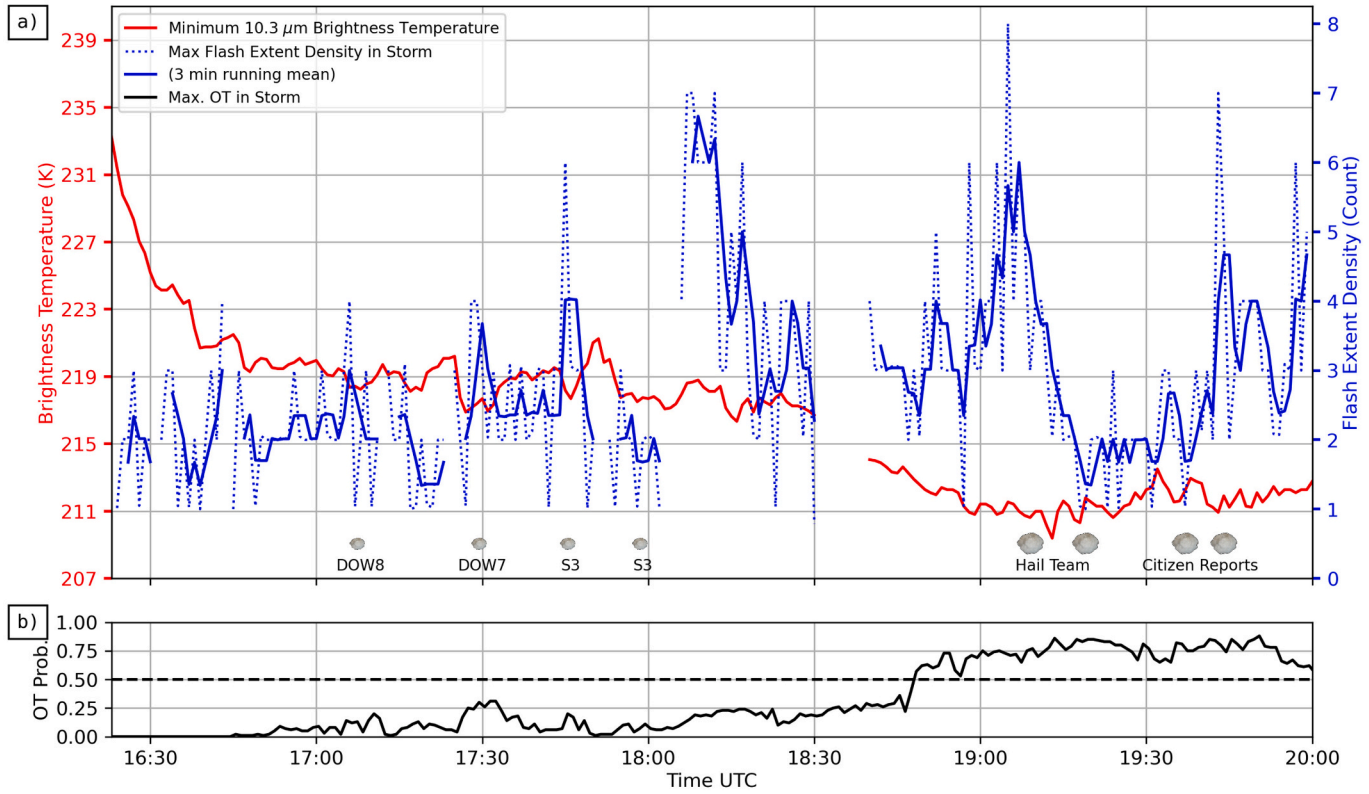

Fig. 14. Time series of a) minimum 10.3 μm brightness temperature in the storm (red), GLM maximum flash extent density (blue), and b) maximum Overshooting Top probability in the storm (black). The hailstone icons indicate the time of hail reports and their sources (small for sub-severe and big for severe reports). (For interpretation of the references to colour in this figure legend, the reader is referred to the web version of this article.)

lightning jumps from GLM, since the detection efficiency (DE) of space-based lightning detectors may be affected by factors including the height of the discharge and the distribution of the scatterers inside the cloud, among others (Brunner and Bitzer, 2020). Furthermore, Rutledge et al. (2020) demonstrated that the GLM DE is particularly low in storms that have low mean flash heights and significant precipitation and cloud water and cloud ice contents. They suggest that optical scattering associated with large cloud ice contents reduces the light intensity at cloud top levels, diminishing the GLM DE on those types of storms. A recent analysis of a severe supercell observed on the Córdoba domain during this field campaign analyzed in Borque et al. (2020) agrees with their findings. Little is known about the electrical characteristics of the storms that affect Mendoza, and although the results shown here are promising, further research based on a larger sample of severe and non-severe storms is needed to properly evaluate the capabilities of using GLM FED as a proxy for severe hail detection in the region. In general, the temporal evolution of the storm characteristics shows some resemblance to those found in Wapler (2017) for their analysis of severe hailstorms in Germany. This includes the increase in pulsing lightning activity prior to cell intensification and the mesocyclone signature in radar data prior to the severe hail reports at the surface.

8. Conclusions

The RELAMPAGO-CACTI field campaign provides a unique opportunity for severe weather research in Argentina. In particular, this was the first time that a severe hailstorm in Mendoza was measured by the multiple observing platforms available during IOP #10. It is also the first study to analyze the characteristics of a supercell and its environment in Mendoza with the level of detail that is only possible thanks to the resources provided by a field campaign of this magnitude.

The data collected during IOP #10 allows us to provide a complete characterization of the storm evolution and environment, which together with the multiple hail reports along the trajectory of the storm are very useful to understand the different processes that act to modulate the storm initiation and severity. Analysis of the pre-convective environment reveals that the development of an upslope flow, in combination with the eroding of the cap by means of the diurnal heating and advancing shortwave trough, provide the conditions for CI over the slope of the terrain. Increased deep-layer shear and CAPE as the storms move away from the mountain range favours the transition into a supercell in which the wider and stronger updraft supports severe hail formation.

The combination of the available in-situ and hailpad reports, along with estimations from the radar HID algorithm, shows that although small hail is observed at the initial stages of the storm, it is only after the transition into a supercell that severe hail of diameter up to 4.5 cm is supported. Examination of GLM maximum FED showed that this transition is preceded by a significant increase in lightning activity, suggesting that this product has some potential for its use in lightning jump algorithms that could be used as a nowcasting tool. The storm also developed an overshooting top signature that was detectable by the automatic algorithm previous to the time of the most severe hail. This automatic overshooting top algorithm also proves to be an effective tool in identifying the more severe phase of the storm, although it fails at pinpointing the occurrence of small hail in the early stages of the storm.

Drawing general conclusions from a single case study is a difficult task. However, the opportunities in which it is possible to sample a storm in the region with the number of observational platforms that were available during the RELAMPAGO campaign are rare. Furthermore, as mentioned earlier, there are no polarimetric radars in the region (important for radar hail detection and convection mode characterization) and hence the analysis of the RELAMPAGO data set is novel too in this sense. It is for these reasons that we think that it is

important to present these kinds of observations that are unique and are not foreseen to be repeated in the near future in Argentina.

Also, the nowcasting techniques (including the HID algorithm) presented in this paper, while not a novelty, have not been tested in storms in this particular region. It is true that the coexistence of an increase in the observed lightning activity or an overshooting top signature in association with the largest hail in this particular storm does not mean that other severe hail storms may behave similarly. In addition, although recent research (Zhou et al., 2021) shows that the environmental conditions in which hailstorms develop share some similarities in some regions of the world, those conditions may vary significantly even within those regions, making it difficult to generalize the results from a single case study. However, we think that a case study with the number of observations presented here is a good starting point from where much more extensive studies, some of them ongoing, may benefit.

The experience leads us to believe that the case study presented here is fairly representative of the severe storms that repeatedly affect the San Rafael region. In particular, the storm studied here initiates and propagates along one of the main storm tracks identified with local radar data in Rosenfeld et al. (2006) (see their Fig. 1). Those storms, like the one presented here, are often severe. The Rosenfeld et al. (2006) work shows that during the 2000–2003 hail seasons in Mendoza (from 15-Oct to 31-Mar), 60% of the days had storms, 18% of the days had hailstorms, and 8% had hailstorms with hail > 2 cm.

Unfortunately, as have been mentioned, most of the previous papers in the region do not address in depth the topic of convection organization, due to the lack of high-quality radar data, nor assess the vertical wind shear when analyzing large samples of hailstorms in the Mendoza province. It is interesting that in most of the papers cited here that analyzed hailstorms in Mendoza the word “supercell” is only mentioned in one of them (Makitov, 1999), in the context of evaluating a hail suppression technique. This is likely a result of the impossibility to detect the rotation associated with supercells with the available non-doppler operational radars. Another exception to this trend of not analyzing convection organization in Mendoza is the García-Ortega et al. (2009) work. García-Ortega et al. (2009) presents two cases that are considered typical situations of deep convection in Mendoza by the DACC sources cited in the article. Both cases are very similar to the one shown here. In particular, the first one is a case where convection evolved into a linear Mesoscale Convective System according to the authors. Looking at the radar data presented in their Fig. 3, in its initial phase (when the convection affects the San Rafael area with hailstones up to 3-cm diameter), the convection appears to be rather isolated, and the general shape of the radar echo certainly looks like it may belong to a supercell. It is after the storm moves eastward that upscale growth is observed, just as it happened during IOP #10. The synoptic pattern associated with those storms is also very similar to what is shown in Figs. 2 and 3, with a shortwave trough entering from the Pacific with negative thermal advection, lee troughing at the surface and upslope flow favouring convection initiation east of the Andes.

The results presented here demonstrate that the transition of a storm into a supercell conditioned its severity, and the size of the hail observed at the surface. This is also suggested by some of the results of previous work, although in most of the published bibliography available online the focus is primarily made on the effects of the enhanced vertical velocity produced by mountain waves in favouring the development of hailstorms in the region, or in demonstrating the effectivity of hail suppression techniques. With that in mind, and in order to determine at which point the results obtained here may be extrapolated to other situations, it is important to advance in the characterization of the convective mode of the storms that affect the Mendoza province. This should definitely require the installation of radars with Doppler capabilities, that allow the detection of rotation within those storms, to complement the current operational network.

Declaration of Competing Interest

The authors declare that they have no known competing financial interests or personal relationships that could have appeared to influence the work reported in this paper.

Acknowledgments

The present work was supported by the projects from Argentina ANPCyT PICT 2017-0221 and PICT 2016- 0710, UBACyT 20020130100618BA, the International cooperation project from Argentina, and CONICET—NSF 2356/18. Authors would like to thanks to Dirección de Agricultura y Contingencias Climáticas, Dr. Alejandro de la Torre and Gabriel Pessano for providing hailpad observations during the event. Thanks also to Ministerio de Educación, Secretaría de Políticas Universitarias Res 2018-29 and INVAP S.E. for their contributions to allow researchers and student participation in the field campaign.

References

Bang, S.D., Cecil, D.J., 2019. Constructing a multifrequency passive microwave hail retrieval and climatology in the gpm domain. J. Appl. Meteorol. Climatol. 58, 1889–1904. URL:

Bedka, K., Brunner, J., Dworak, R., Feltz, W., Otkin, J., Greenwald, T., 2010. Objective satellite-based detection of overshooting tops using infrared window channel brightness temperature gradients. J. Appl. Meteorol. Climatol. 49, 181–202. URL: https://journals.ametsoc.org/view/journals/apme/49/2/2009jamc2286.1.xml https://doi.org/10.1175/2009JAMC2286.1.

Borque, P., Vidal, L., Rugna, M., Lang, T.J., Nicora, M.G., Nesbitt, S.W., 2020. Distinctive signals in 1-min observations of overshooting tops and lightning activity in a severe supercell thunderstorm. J. Geophys. Res. Atmos. 125 https://doi.org/10.1029/2020JD032856 e2020JD032856. URL: https://agupubs.onlinelibrary.wiley.com/doi/abs/10.1029/2020JD032856. E2020JD032856 2020JD032856.

Bosilovich, M.G., Akella, S., Coy, L., Cullather, R., Draper, C., Gelaro, R., Kovach, R., Liu, Q., Molod, A., Norris, P., et al., 2015. Merra-2: Initial Evaluation of the Climate.

Browning, K.A., Foote, G.B., 1976. Airflow and hail growth in supercell storms and some implications for hail suppression. Q. J. R. Meteorol. Soc. 102, 499–533. URL:

Bruick, Z.S., Rasmussen, K.L., Cecil, D.J., 2019. Subtropical south american hailstorm characteristics and environments. Mon. Weather Rev. 147, 4289–4304. URL:

Brunner, K.N., Bitzer, P.M., 2020. A first look at cloud inhomogeneity and its effect on lightning optical emission. Geophys. Res. Lett. 47 https://doi.org/10.1029/2020GL087094 e2020GL087094. E2020GL087094. URL: https://agupubs.onlinelibrary.wiley.com/doi/abs/10.1029/2020GL087094.

Cancelada, M., Salio, P., Vila, D., Nesbitt, S.W., Vidal, L., 2020. Backward adaptive brightness temperature threshold technique (bab3t): a methodology to determine extreme convective initiation regions using satellite infrared imagery. Remote Sens. 12 https://doi.org/10.3390/rs12020337. URL: https://www.mdpi.com/2072-4292/12/2/337.

Casaretto, G., Dillon, M.E., Salio, P., Skabar, Y.G., Nesbitt, S.W., Schumacher, R.S., García, C.M., Catalini, C., 2022. High-resolution nwp forecast precipitation comparison over complex terrain of the sierras de córdoba during relampago-cacti. Weather Forecast. 37, 241–266. URL:

Cecil, D.J., Blankenship, C.B., 2012. Toward a global climatology of severe hailstorms as estimated by satellite passive microwave imagers. J. Clim. 25, 687–703. URL:

de la Torre, A., Daniel, V., Tailleux, R., Teitelbaum, H., 2004. A deep convection event above the tunuyán valley near the andes mountains. Mon. Weather Rev. 132, 2259–2268. https://doi.org/10.1175/1520-0493(2004)132<2259:ADCEAT>2.0.CO;2. URL: https://journals.ametsoc.org/view/journals/mwre/132/9/1520-0493_2004_132_2259_adceat_2.0.co_2.xml.

de la Torre, A., Hierro, R., Llamedo, P., Rolla, A., Alexander, P., 2011. Severe hailstorms near southern Andes in the presence of mountain waves. Atmos. Res. 101, 112–123. URL:

de la Torre, A., Pessano, H., Hierro, R., Santos, J., Llamedo, P., Alexander, P., 2015. The influence of topography on vertical velocity of air in relation to severe storms near the southern Andes mountains. Atmos. Res. 156, 91–101. URL:

Dolan, B., Rutledge, S.A., Lim, S., Chandrasekar, V., Thurai, M., 2013. A robust c-band hydrometeor identification algorithm and application to a long-term polarimetric radar dataset. J. Appl. Meteorol. Climatol. 52, 2162–2186. URL:

García-Ortega, E., López, L., Sánchez, J., 2009. Diagnosis and sensitivity study of two severe storm events in the southeastern Andes. Atmos. Res. 93, 161–178. URL:

Goodman, S.J., Blakeslee, R.J., Koshak, W.J., Mach, D., Bailey, J., Buechler, D., Carey, L., Schultz, C., Bateman, M., McCaul, E., Stano, G., 2013. The goes-r geostationary lightning mapper (glm). Atmos. Res. 125–126, 34–49. URL: https://www.sciencedirect.com/science/article/pii/S0169809513000434. https://doi.org/10.1016/j.atmosres.2013.01.006.

Goodman, S., Schmit, T., Daniels, J., Redmon, R., 2019. The GOES-R Series. Elsevier.

Grandoso, H.N., Iribarne, J.V., 1963. Evaluation of the first three years in a hail prevention experiment in mendoza (argentina). Zeitschrift für angewandte Mathematik und Physik ZAMP 14, 549–553. https://doi.org/10.1007/BF01601262.

Helmus, J.J., Collis, S.M., 2016. The python arm radar toolkit (py-art), a library for working with weather radar data in the python programming language. J. Open Res. Softw. 4.
Hierro, R., Pessano, H., Llamedo, P., de la Torre, A., Alexander, P., Odiard, A., 2013. Orographic effects related to deep convection events over the Andes region. Atmos. Res. 120-121, 216–225. URL:
Hong, S.-Y., Noh, Y., Dudhia, J., 2006. A new vertical diffusion package with an explicit treatment of entrainment processes. Mon. Weather Rev. 134, 2318–2341. URL: https://journals.ametsoc.org/view/journals/mwre/134/9/mwr3199.1.xml https://doi.org/10.1175/MWR3199.1.
Iacono, M.J., Delamere, J.S., Mlawer, E.J., Shephard, M.W., Clough, S.A., Collins, W.D., 2008. Radiative forcing by long-lived greenhouse gases: Calculations with the aer radiative transfer models. J. Geophys. Res. Atmos. 113 https://doi.org/10.1029/2008JD009944. URL: https://agupubs.onlinelibrary.wiley.com/doi/abs/10.1029/2008JD009944.
Kain, J.S., Weiss, S.J., Bright, D.R., Baldwin, M.E., Levit, J.J., Carbin, G.W., Schwartz, C. S., Weisman, M.L., Droegemeier, K.K., Weber, D.B., Thomas, K.W., 2008. Some practical considerations regarding horizontal resolution in the first generation of operational convection-allowing nwp. Weather Forecast. 23, 931–952. URL:
Khlopenkov, K.V., Bedka, K.M., Cooney, J.W., Itterly, K., 2021. Recent advances in detection of overshooting cloud tops from longwave infrared satellite imagery. J. Geophys. Res. Atmos. 126 https://doi.org/10.1029/2020JD034359 e2020JD034359. URL: https://agupubs.onlinelibrary.wiley.com/doi/abs/10.1029/2020JD034359. E2020JD034359 2020JD034359.
Kumjian, M.R., Lombardo, K., 2020. A hail growth trajectory model for exploring the environmental controls on hail size: Model physics and idealized tests. J. Atmos. Sci. 77, 2765–2791. URL:
Kumjian, M.R., Gutierrez, R., Soderholm, J.S., Nesbitt, S.W., Maldonado, P., Luna, L.M., Marquis, J., Bowley, K.A., Imaz, M.A., Salio, P., 2020. Gargantuan hail in argentina. Bull. Am. Meteorol. Soc. 101, E1241–E1258. URL:
Makitov, V., 1999. Organization and main results of the hail suppression program in the northern area of the province of mendoza, argentina. J. Wea. Modif. 31, 76–86.
Marengo, J.A., Soares, W.R., Saulo, C., Nicolini, M., 2004. Climatology of the low-level jet east of the Andes as derived from the ncep–ncar reanalyses: Characteristics and temporal variability. J. Clim. 17, 2261–2280. https://doi.org/10.1175/1520-0442(2004)017<2261:COTLJE>2.0.CO;2.
Markowski, P., Richardson, Y., 2010. Mesoscale Meteorology in Midlatitudes. John Wiley and Sons. https://doi.org/10.1002/9780470682104.
Matsudo, C., Salio, P., 2011. Severe weather reports and proximity to deep convection over northern argentina. Atmos. Res. 100, 523–537. URL: https://www.sciencedirect.com/science/article/pii/S0169809510003078 https://doi.org/10.1016/j.atmosres.2010.11.004, 5th European Conference on Severe Storms.
Mezher, R.N., Doyle, M., Barros, V., 2012. Climatology of hail in argentina. Atmos. Res. 114-115, 70–82. URL:
Mulholland, J.P., Nesbitt, S.W., Trapp, R.J., Rasmussen, K.L., Salio, P.V., 2018. Convective storm life cycle and environments near the sierras de córdoba, argentina. Mon. Weather Rev. 146, 2541–2557. URL:
Nesbitt, S.W., Salio, P.V., Ávila, E., Bitzer, P., Carey, L., Chandrasekar, V., Deierling, W., Dominguez, F., Dillon, M.E., Garcia, C.M., Gochis, D., Goodman, S., Hence, D.A., Kosiba, K.A., Kumjian, M.R., Lang, T., Luna, L.M., Marquis, J., Marshall, R., McMurdie, L.A., Nascimento, E.L., Rasmussen, K.L., Roberts, R., Rowe, A.K., Ruiz, J. J., Sabbas, E.F.S., Saulo, A.C., Schumacher, R.S., Skabar, Y.G., Machado, L.A.T., Trapp, R.J., Varble, A., Wilson, J., Wurman, J., Zipser, E.J., Arias, I., Bechis, H., Grover, M.A., 2021. A storm safari in subtropical south america: proyecto relampago. Bull. Am. Meteorol. Soc. 1–64. URL:
Pérez, R.C., Puliafito, E., 2006. Study of Hailstorms Cells Producing Big Damages in mendoza (argentina). Proc. Fourth European Conf. on Radar in Meteorology and Hydrology, Barcelona, Spain, ERAD, 4 pp. URL: http://www.crahi.upc.edu/ERAD2006/proceedingsMask/00136.pdf.
Peterson, M., 2021. Where are the most extraordinary lightning megaflashes in the americas? Bull. Am. Meteorol. Soc. 102, E660–E671. URL. https://journals.ametsoc.org/view/journals/bams/102/3/BAMS-D-20-0178.1.xml. https://doi.org/10.1175/BAMS-D-20-0178.1.
Rasmussen, K.L., Houze, R.A., 2016. Convective initiation near the andes in subtropical south america. Mon. Weather Rev. 144, 2351–2374. URL:
Rauber, R.M., Nesbitt, S.W., 2018. Radar Meteorology. John Wiley and Sons, Ltd.
Rosenfeld, D., Woodley, W.L., Krauss, T.W., Makitov, V., 2006. Aircraft microphysical documentation from cloud base to anvils of hailstorm feeder clouds in argentina. J. Appl. Meteorol. Climatol. 45, 1261–1281. URL:
Rutledge, S.A., Hilburn, K.A., Clayton, A., Fuchs, B., Miller, S.D., 2020. Evaluating geostationary lightning mapper flash rates within intense convective storms. J. Geophys. Res. Atmos. 125 https://doi.org/10.1029/2020JD032827 e2020JD032827. URL: https://agupubs.onlinelibrary.wiley.com/doi/abs/10.1029/2020JD032827.
Salio, P., Nicolini, M., Saulo, A.C., 2002. Chaco low-level jet events characterization during the austral summer season. J. Geophys. Res. Atmos. 107 https://doi.org/10.1029/2001JD001315. ACL 32–1–ACL 32–17. URL: https://agupubs.onlinelibrary.wiley.com/doi/abs/10.1029/2001JD001315.
Salio, P., Nicolini, M., Zipser, E.J., 2007. Mesoscale convective systems over Southeastern South America and their relationship with the South American low-level jet. Mon. Weather Rev. 135, 1290–1309. https://doi.org/10.1175/MWR3305.1.
Sánchez, J.L., Marcos, J.L., Dessens, J., López, L., Bustos, C., García-Ortega, E., 2009. Assessing sounding-derived parameters as storm predictors in different latitudes. Atmos. Res. 93, 446–456. URL:
Saulo, C., Ferreira, L., Nogués-Paegle, J., Seluchi, M., Ruiz, J., 2010. Land–atmosphere interactions during a northwestern argentina low event. Mon. Weather Rev. 138, 2481–2498. https://doi.org/10.1175/2010MWR3227.1.
Schultz, C.J., Petersen, W.A., Carey, L.D., 2011. Lightning and severe weather: a comparison between total and cloud-to-ground lightning trends. Weather Forecast. 26, 744–755. URL:
Seluchi, M.E., Saulo, A.C., Nicolini, M., Satyamurty, P., 2003. The northwestern argentinean low: a study of two typical events. Mon. Weather Rev. 131, 2361–2378. https://doi.org/10.1175/1520-0493(2003)131<2361:TNALAS>2.0.CO;2.
Skamarock, W.C., Klemp, J.B., Dudhia, J., Gill, D.O., Liu, Z., Berner, J., Wang, W., Powers, J.G., Duda, M.G., Barker, D.M., et al., 2019. A description of the advanced research wrf model version 4. Natl Cent. Atmos. Res. Boulder, CO, USA 145, 145.
Soderholm, J.S., Kumjian, M.R., McCarthy, N., Maldonado, P., Wang, M., 2020. Quantifying hail size distributions from the sky – application of drone aerial photogrammetry. Atmos. Meas. Tech. 13, 747–754. URL:
Teitelbaum, H., D'Andrea, F., 2015. Deep convection east of the Andes cordillera: four hailstorm cases. Tellus A: Dyn. Meteorol. Oceanogr. 67, 26806 https://doi.org/10.3402/tellusa.v67.26806.
Testud, J., Bouar, E.L., Obligis, E., Ali-Mehenni, M., 2000. The rain profiling algorithm applied to polarimetric weather radar. J. Atmos. Ocean. Technol. 17, 332–356. https://doi.org/10.1175/1520-0426(2000)017<0332:TRPAAT>2.0.CO;2. URL: https://journals.ametsoc.org/view/journals/atot/17/3/1520-0426_2000_017_0332_trpaat_2_0_co_2.xml.
Thompson, G., Field, P.R., Rasmussen, R.M., Hall, W.D., 2008. Explicit forecasts of winter precipitation using an improved bulk microphysics scheme. part ii: Implementation of a new snow parameterization. Mon. Weather Rev. 136, 5095–5115. URL:
Varble, A.C., Nesbitt, S.W., Salio, P., Hardin, J.C., Bharadwaj, N., Borque, P., DeMott, P. J., Feng, Z., Hill, T.C.J., Marquis, J.N., Matthews, A., Mei, F., Öktem, R., Castro, V., Goldberger, L., Hunzinger, A., Barry, K.R., Kreidenweis, S.M., McFarquhar, G.M., McMurdie, L.A., Pekour, M., Powers, H., Romps, D.M., Saulo, C., Schmid, B., Tomlinson, J.M., van den Heever, S.C., Zelenyuk, A., Zhang, Z., Zipser, E.J., 2021. Utilizing a storm-generating hotspot to study convective cloud transitions: the cacti experiment. Bull. Am. Meteorol. Soc. 1–67. URL:
Vera, C., Baez, J., Douglas, M., Emmanuel, C.B., Marengo, J., Meitin, J., Nicolini, M., Nogues-Paegle, J., Paegle, J., Penalba, O., Salio, P., Saulo, C., Dias, M.A.S., Dias, P.S., Zipser, E., 2006. The south american low-level jet experiment. Bull. Am. Meteorol. Soc. 87, 63–78. URL:
Wapler, K., 2017. The life-cycle of hailstorms: Lightning, radar reflectivity and rotation characteristics. Atmos. Res. 193, 60–72. URL: https://www.sciencedirect.com/science/article/pii/S0169809516306020 https://doi.org/10.1016/j.atmosres.2017.04.009.
Whiteman, C.D., 2000. Mountain Meteorology: Fundamentals and Applications. Oxford University Press.
Wurman, J., Straka, J., Rasmussen, E., Randall, M., Zahrai, A., 1997. Design and deployment of a portable, pencil-beam, pulsed, 3-cm doppler radar. J. Atmos. Ocean. Technol. 14, 1502–1512. https://doi.org/10.1175/1520-0426(1997)014<1502:DADOAP>2.0.CO;2. URL: https://journals.ametsoc.org/view/journals/atot/14/6/1520-0426_1997_014_1502_dadoap_2_0_co_2.xml.
Zhou, Z., Zhang, Q., Allen, J. T., Ni, X., & Ng, C.-P. (2021). How many types of severe hailstorm environments are there globally? Geophys. Res. Lett., 48, e2021GL095485. URL: https://agupubs.onlinelibrary.wiley.com/doi/abs/10.1029/2021GL095485. doi: https://doi.org/10.1029/2021GL095485. arXiv:https://agupubs.onlinelibrary.wiley.com/doi/pdf/10.1029/2021GL095485. E2021GL095485 2021GL095485.
Zipser, E.J., Cecil, D.J., Liu, C., Nesbitt, S.W., Yorty, D.P., 2006. Where are the most intense thunderstorms on earth? Bull. Am. Meteorol. Soc. 87, 1057–1072. URL.
Zrnić, D.S., 1987. Three-body scattering produces precipitation signature of special diagnostic value. Radio Sci. 22, 76–86. https://doi.org/10.1029/RS022i001p00076.